journal of the mechanical behavior of biomedical materials 160 (2024) 106791

Contents lists available at ScienceDirect

Journal of the Mechanical Behavior of Biomedical Materials

journal homepage: www.elsevier.com/locate/jmbbm

Bio-inspired space-filling fractal metamaterial

Tiantian Li, Yaning Li *

Department of Mechanical and Industrial Engineering, Northeastern University, Boston, USA

ARTICLE INFO

Keywords:
Bio-inspired
Space-filling fractal
3D printing
Metamaterial

ABSTRACT

Inspired by mammal cranial sutures with spatiotemporal morphological variation, two-phase space-filling fractal metamaterial was designed. Designs with different levels of complexity are fabricated via multi-material polymer jetting. Mechanical tests and systematic finite element (FE) simulations are conducted to evaluate the mechanical performance of the designs. It is found that the hierarchical number *N* of two-phase space-filling fractal metamaterial played an important role in their mechanical behaviors. The experimental results show that with increasing the hierarchical number *N*, these metamaterials show enhanced stiffness, strength, and toughness under tensile tests. From the simulation results, we found by decoupling the strain energy density in two phases, with increasing *N*, the soft phase has contributed almost the same energy level, however, the hard phase has contributed increasing energy level. Moreover, we found the volume fraction and the stiffness ratio of the hard phase dominate the overall mechanical properties of these two-phase space-filling fractal metamaterial. The bio-inspired mechanical metamaterials have broad applications in engineering materials for dissipating energy dissipation, mitigating impact, and retarding damages.

1. Introduction

Natural materials often feature intricate geometries that play a crucial role in their mechanical performance, inspiring engineers to create new materials (Dunlop et al., 2011; Meyers et al., 2008; Wainwright, 1982). These geometries often exhibit hierarchy across different scales, showcasing complex, fractal-like patterns with repeated self-similar shapes (Long and Long, 2008; Saunders et al., 1999; Yao and Gao, 2006; Zhou and Zhang, 2005). Such hierarchical designs are known to significantly enhance the mechanical properties of natural materials (Jaslow, 1990; Jaslow and Biewener, 1995). Man-made hierarchical and fractal metamaterials via additive manufacturing also exhibit enhanced mechanical properties (Martínez-Magallanes et al., 2023, 2024; Zhang et al., 2023). An intriguing example of hierarchical design in nature is seen in suture interfaces, which consist of compliant, interlocking seams connecting stiffer components (Jaslow, 1990; Krauss et al., 2009; Landman et al., 2007; Li et al., 2011; Saunders et al., 1999; Sun et al., 2004). Biological suture morphologies are versatile, such as wavy cranial sutures in human skulls (Song et al., 2010), the elaborate hierarchical designs seen in ammonites (Li et al., 2012; Saunders and Work, 1996), the 3D interdigitations in turtle shell (Alheit et al., 2020; Wang et al., 2021).

Mechanics of suture interfaces have been studied via experiments and finite element analysis (FEA). It has been found that suture interfaces can provide uniform stress distribution (Li et al., 2011), enhanced energy absorption (Jaslow, 1990), compliance (Hubbard et al., 1971), deformability (Dunlop et al., 2011), flexibility (Herring, 2008; Krauss et al., 2009), and damping behavior (Cui et al., 2021). Moreover, bio-inspired sutural tessellation was shown to play an important role in amplifying strength, toughness, and authenticity (Cao et al., 2019; Gao et al., 2018). These studies confirm that geometric variation affects the effective mechanical behavior of the sutures.

Interestingly, morphologies of cranial sutures for mammals with horns show spatiotemporal variation. For example, for Shetland sheep, the cranial sutures show spatial variation in complexity, as shown in Fig. 1a, exhibiting a more complicated space-filling type of morphology between the horns. The different suture complexity at different locations can be conceptually represented by a simple rectangular wave (Fig. 1b and c) vs. a space-filling curve, such as the Hilbert curve (Fig. 1d and e). Also, dear cranial sutures show age-dependent geometries (Nicolay and Vaders, 2006). In adult-age deer (>4 years), cranial sutures show a much more complicated morphology than those in young-age deer (<1.5 years). Although this spatiotemporal variation in cranial sutures is well observed and recorded, it is not clear how the variation in suture morphology is quantitatively related to the mechanical performance and functions of sutures.

* Corresponding author.
E-mail address: y.li@northeastern.edu (Y. Li).

https://doi.org/10.1016/j.jmbbm.2024.106791
Received 13 June 2024; Received in revised form 3 August 2024; Accepted 28 October 2024
Available online 29 October 2024

In this paper, we design a new family of space-filling fractal metamaterial which is inspired by the complex microstructures of cranial sutures of mammals. A multi-material 3D printer (Stratasys Connex 3) is used to fabricate the designs. Uni-axial tension tests are performed to evaluate their mechanical performance. Also, systematic finite element (FE) simulations are conducted to explore the effects of hierarchy number, stiffness ratio of multi-material, and volume fraction of each phase on the overall mechanical properties of the designs.

2. Space-filling fractal sutures design

2.1. Hilbert's space-filling curve

Hilbert space-filling curve was first defined by the German mathematician David Hilbert in 1891 (Hilbert, 1891). It is one of the space-filling, self-avoiding, simple (single stroke), and self-similar (FASS) curves. It is generated via a recursive algorithm: the seed of the Hilbert space-filling curve is an upside-down U-shape at hierarchy level $N = 1$, as shown in Fig. 2a. To create the Hilbert space-filling curve of $N = 2$, the seed curve of $N = 1$ repeats twice on the top row and rotates 90° clockwise and counterclockwise at the bottom row, respectively, as shown in Fig. 2b. By connecting these four seed sections with three straight lines (blue), the Hilbert curve with $N = 2$ is constructed. By repeating this process, a group of Hilbert space-filling curves is constructed with the hierarchy number N. The examples with $N = 1$ to 6 are shown in Fig.2a-e, respectively. By assuming the edge length of the square as 1, the total length of the Hilbert curve with N is $2^N - \frac{1}{2^N}$ (Hilbert, 1891). The total length grows exponentially with N, while the filling area is kept close to a constant, as shown in Fig. 2.

2.2. Two-phase space-filling fractal metamaterial

By assigning a thickness t to the Hilbert curves, the space-filling curve becomes a space-filling layer. Defining the layer as a domain with a different material property from the matrix domain outside the layer, a two-phase space-filling fractal metamaterial is obtained. For this type of metamaterial with hierarchical number N, the layer thickness is t_N. Here, each sample contains two repeated units arranged in a horizontal direction. Both curves are connected in the center and extended to the edges. Therefore, the metamaterial includes three parts: the top part, the center part of the fractal layer, and the bottom part. The top and bottom parts are defined as a harder phase and the center part is defined as a softer phase. By changing the thickness of the layer, the volume fractions of hard and soft phases can be adjusted. The thickness of the soft phase, t_N as $t_N = Hf_s/\left(2^N - 1/2^N\right)$, where H is the height of the, $f_s = V_s/V$ is the volume fraction of the soft phase, and N is the hierarchical number. A group of space-filling fractal metamaterials is designed with a hierarchical number N varies from 1 to 5, as shown in Fig. 3.

3. Material and methods

3.1. 3D printing

The prototypes of space-filling fractal metamaterials are fabricated using a multi-material 3D printer Objet Connex3 260. We use two photosensitive polymeric materials, a soft elastomeric material, Agilus 30 (A30), and an acrylic-based photopolymer, VeroWhite (VW). The soft phase is printed with the material of A30 (Young's modulus~0.7 MPa), and the hard bone phase is printed with VW (Young's modulus~1.7 GPa).

The geometry of the 3D printed specimen is shown in Fig. 4a, the design is in the middle, and shoulders are added as VW plates. In the middle design area, the height is $H = 50$ mm, the length is $L = 100$ mm, the out-of-plane thickness is $D = 2$ mm, and the thickness of shoulder plates is $D_1 = 4$ mm. The thicker shoulder plates are used to reduce the boundary effects and facilitate homogeneous deformation in the middle design area. To achieve high resolution in the printed specimens, the minimum in-plane layer thickness t_N is ~400 μm, which is one order of magnitude greater than the minimum resolution (16 μm) provided by the 3D printer. All the specimens are printed along the same orientation to avoid the potential influences from the printing direction. The as-fabricated specimens are kept at room temperature for 7 days to allow for the saturation of the curing.

Two groups (G1 and G2) of the specimens are designed and manufactured (the design parameters are summarized in Table 1). The specimens in G1 shown in Fig. 4b-d have the same volume fraction, $f_s = 0.256$ but different numbers of hierarchy $N = 3$, 4, and 5, respectively. The volume fraction of the soft phase is kept at 25%, thus the

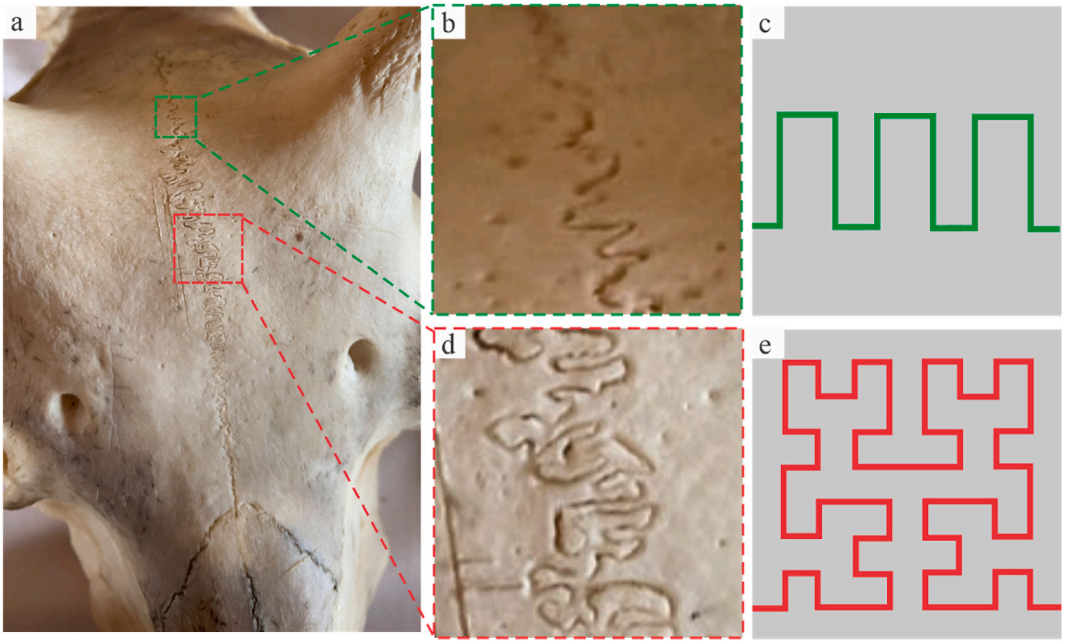

Fig. 1. (a) Shetland sheep skull cranial sutures (b) with a relatively simple zigzag geometry, conceptually represented by a rectangular wave (c), and (d) with a more complete geometry, represented by a 2D space-filling Hilbert curve (f).

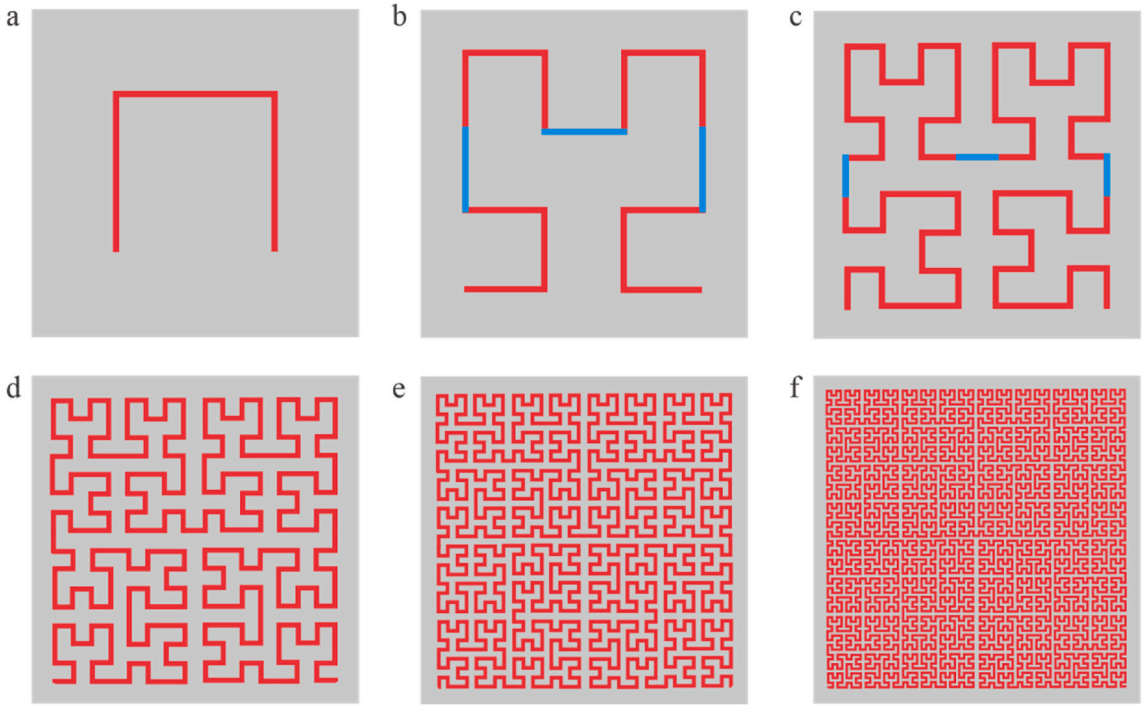

Fig. 2. Hilbert space-filling fractal curves. (a) $N = 1$; (b) $N = 2$; (c) $N = 3$; (d) $N = 4$; (e) $N = 5$; (f) $N = 6$.

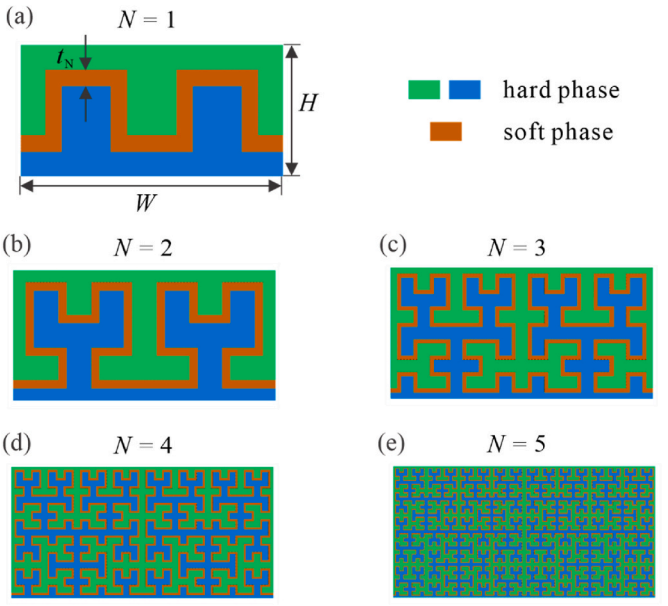

Fig. 3. Space-filling fractal metamaterials. (a) Geometry parameters, and the design of $N = 1$, (b) $N = 2$, (c) $N = 3$, (d) $N = 4$, and (e) $N = 5$.

volume fraction of the hard phase is 75%. The specimens in G2 shown in Fig. 4e-g have the same in-plane thickness of the fractal layer ($t_N = 0.4$ mm) and different N ($N = 3$, 4, and 5, respectively).

3.2. Uniaxial tension experiments

To characterize the effective mechanical properties of the space-filling fractal metamaterials, uniaxial tension experiments are performed on the 3D printed specimens, by using an Instron mechanical testing machine with a 10 kN load cell. All the tests are conducted in a quasi-static regime with a strain rate of 0.001 s^{-1}. A high-resolution camera (Grasshooper3) is used to record the deformed configurations of the specimens at each time instant during the experiments. By post-processing images, the displacement histories of two marked points in the design area are obtained, from which the effective stress-strain curves are calculated.

3.3. Finite element simulations

The numerical simulations of the uniaxial tension experiments are conducted by using the commercial finite element (FE) package ABAQUS/Standard (Simulia, Providence, RI). 2D FE models with plane stress elements (CPS3) are developed. Mesh convergence tests are conducted. Geometric and material nonlinearities are taken into consideration to enable the precise simulation at relatively large deformation. The stress-strain behavior of the hard phase is modeled from the true stress-strain relation of VeroWhite. The elastomeric stress-strain behavior of AgiliusBlack is modeled as a hyperelastic material via Arruda-Boyce hyperelastic model (Arruda and Boyce, 1993) with an initial shear modulus of 0.213 MPa and a locking stretch of 1.9. To simulate the experimental conditions, prescribed uniaxial displacement was applied on the top surface, fixed on the bottom surface, and free on the horizontal surfaces.

4. Experimental results

The experimental results of group G1 are shown in Fig. 5. The engineering stress-strain curves for samples with $N = 3$, 4, and 5 exhibit three deformation stages: elastic deformation, plastic yielding, and failure, as shown in Fig. 5a. Fig. 5a shows that in the elastic stage, when N increases, the stress-strain curves show an increase in slope, indicating a higher effective stiffness. In the plastic yielding stage, the initial yielding stress increases with N. To clearly demonstrate the evolution of deformation, for each specimen four snapshots (Fig.5b-d) are selected to represent the deformation in the elastic stage, plastic yielding, first failure, and final failure, respectively.

For all three samples, at a small overall strain ($\varepsilon = 0.03$), the overall deformation is dominated by the deformation of the soft phase. How-

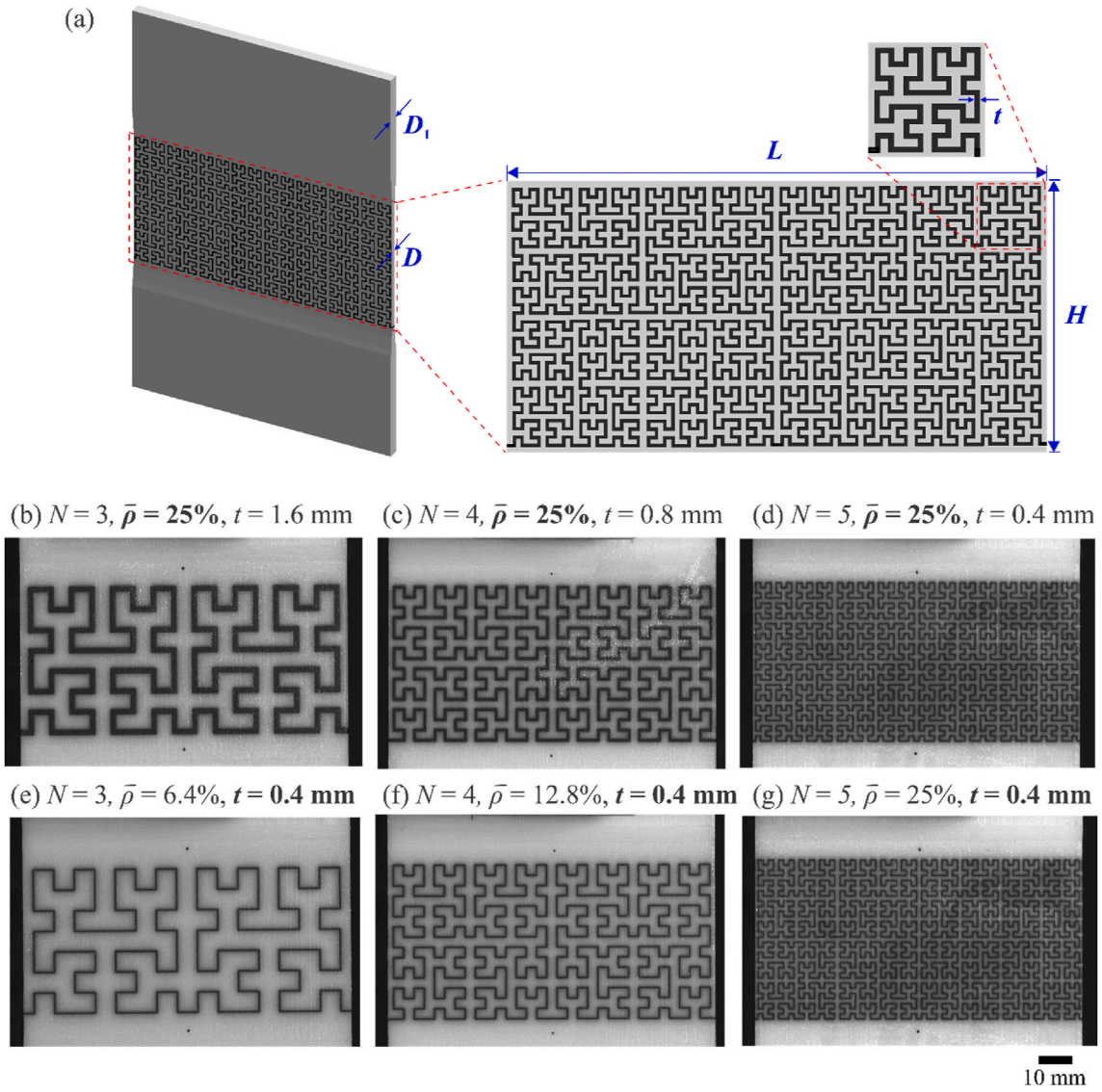

Fig. 4. Designed specimens for tensile tests. (a) Schematics for the geometry parameters of the tensile specimens. 3D printed specimens in group 1 (G1) have the same volume fraction of soft phase (25%) with (b) $N = 3$, (c) $N = 4$, and (d) $N = 5$.3D printed specimens in group 2 (G1) have the same thickness of soft phase (0.4 mm) with (e) $N = 3$, (f) $N = 4$, and (g) $N = 5$.

Table 1
Geometry parameters of experimental samples for tensile tests. Here, the volume fraction of the soft phase is f_s and the thickness of the fractal layer is t_N.

Geometry Parameters	G1			G2		
	N = 3	N = 4	N = 5	N = 3	N = 4	N = 5
f_s	0.256	0.256	0.256	0.064	0.128	0.256
t_N (mm)	1.6	0.8	0.4	0.4	0.4	0.4

ever, different parts of the soft phase are under different deformation modes including compression, tension, or shearing. When the specimens continue to be stretched to a larger overall tensile strain, the soft phases under tension break. The cracks can be noticed and marked with yellow circles in Fig. 5 b1, c1, and d1. At the same time, the deformation in the hard phase increases, and yielding occurs in certain locations in the hard phase. The first failure occurs in the same positions marked in Fig. 5 b3, c3, and d3, followed by crack propagation until a catastrophic failure is shown in Fig. 5 b4, c4, and d4.

The experimental results of specimens in the G2 group are shown in Fig. 6. The engineering stress-strain curves for samples with $N = 3$, 4, and 5 also exhibit three stages: elastic deformation, the plastic yielding, and failure process, as shown in Fig. 6a. Fig. 6a shows that when N increases, both the effective stiffness and yielding stress decrease. This is mainly because when the layer thickness is the same, the total volume fraction of the hard phase decreases with increasing N. For example, when $N = 3$, the design has the largest volume fraction of the hard phase (93.6%) making its property getting closer to the constituent material of the hard phase (VW). For each specimen, the snapshots of the elastic stage, plastic yielding, first failure, and final failure are shown in Fig. 6b-d).

It is noticed that the first failure (Fig. 6a) occurs at a similar strain in the sample with $N = 3$, 4, and 5, respectively. However, the final failure in the sample with $N = 3$ and 4 is catastrophic, indicating a brittle failure mode. Differently, the final failure in the sample with N = 5 shows a progressive failure which indicates a ductile mode. Experimental snapshots (Fig. 6b-d) clearly show that in the stage of failure, when N increases, the final failure becomes more and more graceful. For example, for the design of $N = 5$, the process of *d*3-*d*4 is way more graceful than the processes of *b*3-*b*4, and *c*3-*c*4.

Based on the experimental stress-strain curves, the effective

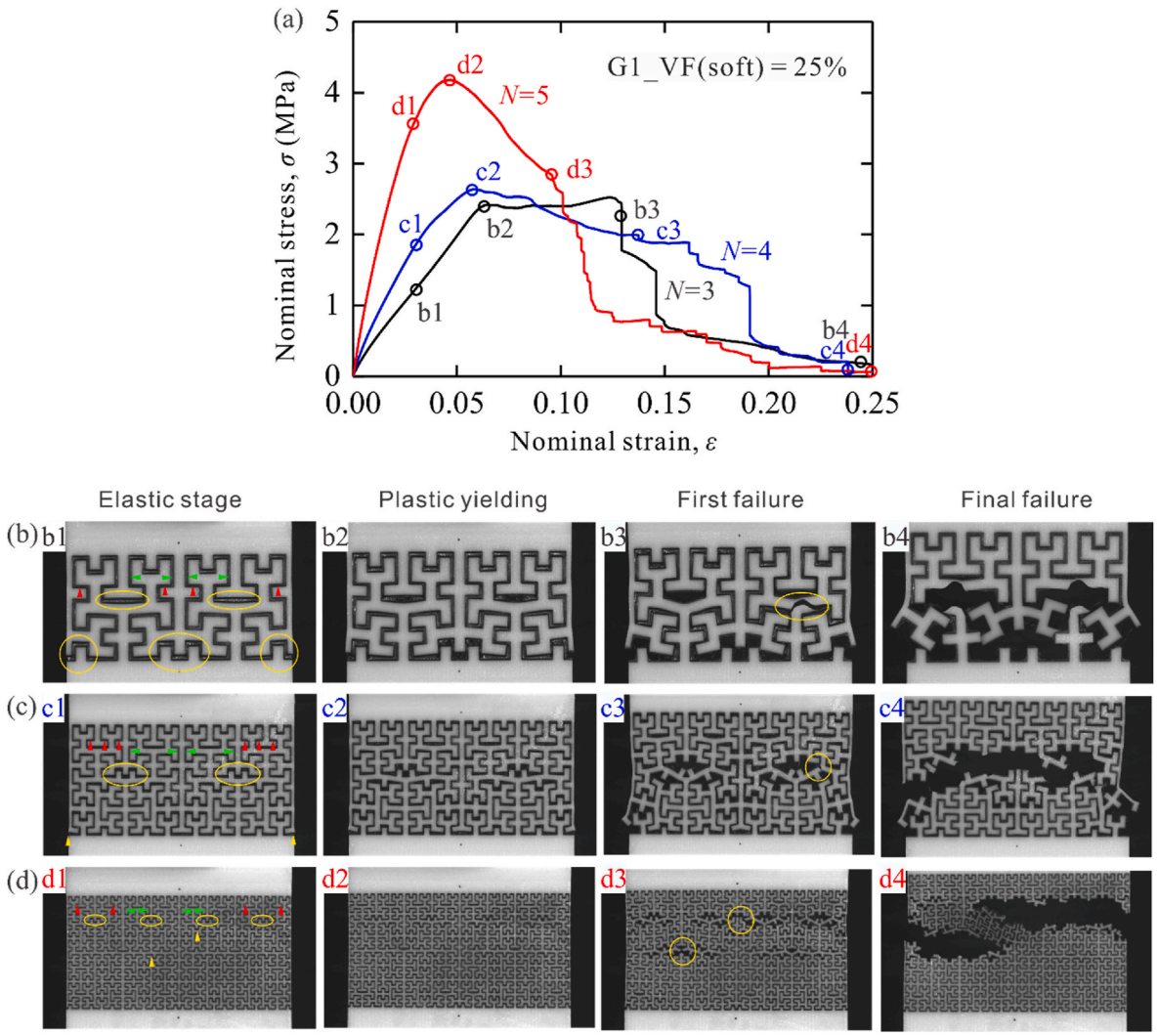

Fig. 5. Experimental results for specimens in group 1 (G1) with the same volume fraction of soft phase (25%). (a) Experimental engineering stress-strain curves, and (b) selected deformation patterns for the sample with $N = 3$, (c) $N = 4$, and (d) $N = 5$. In the soft phase, the deformation of compression (red arrows), shearing (green arrows), tension, and tensile failures (yellow circles or arrows) are marked in selected areas.

mechanical properties including the effective stiffness, strength, and resilience for the G1 and G2 specimens are compared in Fig. 7a-c, respectively. Effective stiffness is defined as the initial slope of the stress-strain curve in the elastic regime. Effective strength is defined as the overall stress at the peak of the stress-strain curve. Resilience is defined as the energy absorbed in the elastic regime.

Fig. 7a and b shows that for designs in group G1, both the effective stiffness and effective strength increase with increasing N, however, for designs in group G2, the trends are opposite. As we explained before, this is dominated by the effects of volume fraction. While for resilience, the designs from both groups show a consistent trend and similar level of values at each N level, resilience increases with increasing N.

5. Results of systematic parametric study

5.1. Effective stiffness of space-filling fractal metamaterial

The mechanical properties of space-filling fractal metamaterials are strongly affected by the material properties of both the hard and soft phases. Especially, the effective stiffness $\bar{E}$ depends on the stiffness ratio, E_h/E_s between hard phase and soft phase. To systematically explore the effects of stiffness ratio E_h/E_s, FE models with $N = 1$-5 in the G1 groups are developed. For all models, the volume fraction of the soft phase is 25%. For the FE models with $N = 1$-5, the in-plane thickness of the soft layer is 0.4, 0.8, 1.6, 3.2, and 6.4 mm, respectively. Then for each FE model, the stiffness of the hard phase is fixed as $E_h = 1.7$ GPa, and the stiffness of the soft phase varies as $E_s = 0.01$, 0.1, 0.7, 1, 3, and 10 MPa. Thus, the stiffness ratio E_h/E_s varies from 1.7×10^2 to 1.7×10^5. A total of 30 FE simulations were conducted.

It is worth mentioning that for the multi-material 3D printer, the effective stiffness of very thin flat soft layers (less than 1 mm) depends on the thickness of the layer (Liu et al., 2020b; Liu and Li, 2018). This is because of material mixing between the soft and the hard phases during printing. A group of specimens of flat layers with in-plane layer thicknesses of 0.4, 0.8, 1.6, 3.2, and 6.4 mm are designed and fabricated. Uni-axial tension experiments are conducted. The effective stress-strain curves are obtained (Fig. 8a).

The effective stiffness of layers with different thicknesses are compared in Fig. 8b. It can be seen that for $t = 1.6$ mm, 0.8 mm, and 0.4 mm, $E_s = 0.7$ MPa, 1 MPa, and 3 MPa, respectively. This is consistent with the values we used in the parametric FE simulations, as shown in Table 2.

The effective stiffness as a function of N and E_s are shown in Fig. 8c and d. First, the results from FE simulations agree well with those from previous experiments. Second, it shows that for a certain E_s, higher hierarchy number N results in higher effective stiffness. With increasing

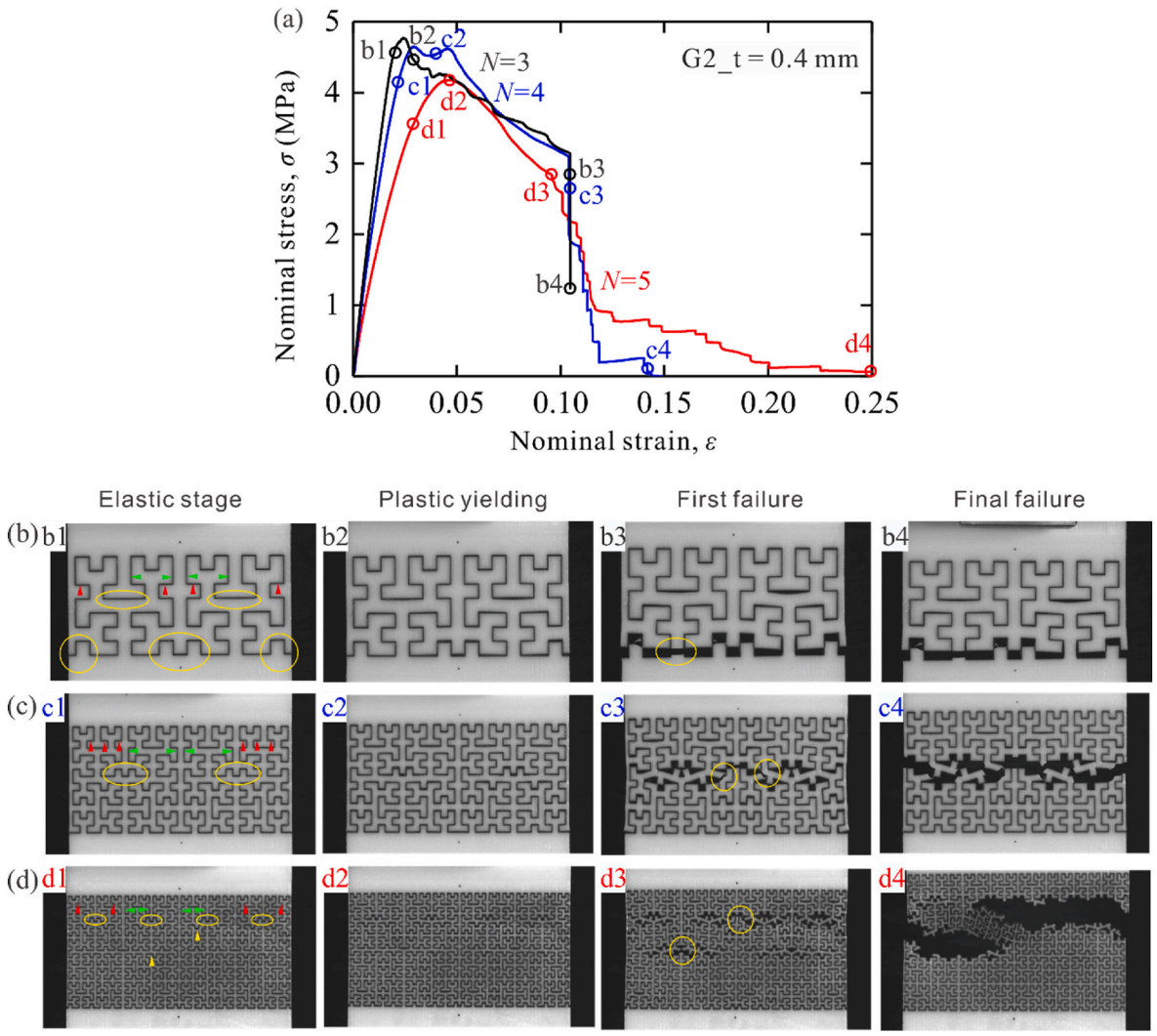

Fig. 6. Experimental results for specimens in group 2 (G2) with the same in-plane thickness (0.4 mm) of the soft phase. (a) Experimental engineering stress-strain curves and the snapshots for the specimens with (b) $N = 3$, (c) $N = 4$, and (d) $N = 5$. In the soft phase, the deformation of compression (red arrows), shearing (green arrows), tension, and tensile failures (yellow circles or arrows) are marked in selected areas.

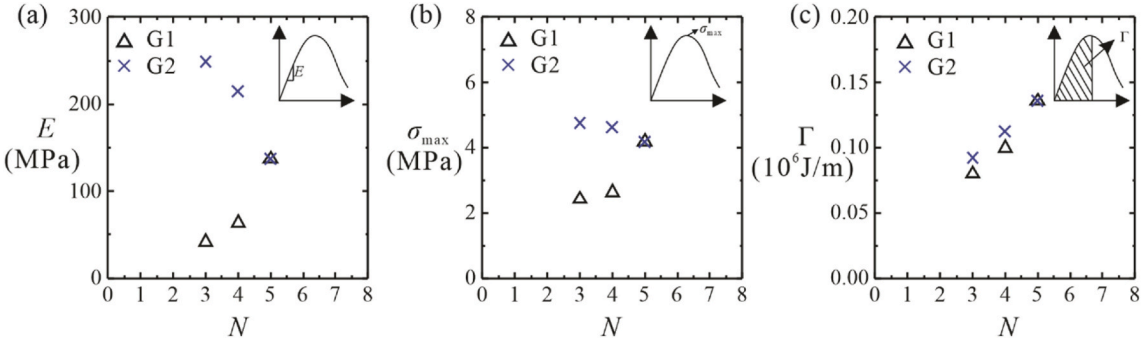

Fig. 7. Measured effective mechanical properties, (a) stiffness, (b) strength, and (c) resilience as functions of the hierarchy number, N.

E_s, the effective stiffness becomes less dependent on N. For example, as shown in Fig. 8c, when $E_s = 0.01$ MPa, the effective stiffness increases from 0.1 MPa to 3 MPa when N increases from 1 to 4. When N increases from 4 to 5, the effective stiffness increases from 3 MPa to 3.5 MPa. In compassion, when $E_s = 10$ MPa, when N increases from 1 to 2, the effective stiffness increases from 75 MPa to 172 MPa. However, when $N \geq 2$, the effective stiffness remains almost unchanged when increasing N.

To further understand the effects of stiffness ratio and N on the effective stiffness, we explored the total strain energy and the strain energy of the hard phase and soft phase, respectively. The relationship between the total strain energy and the overall stiffness is:

$$U = \frac{1}{2}\bar{E}\bar{\varepsilon}^2 V. \quad (1)$$

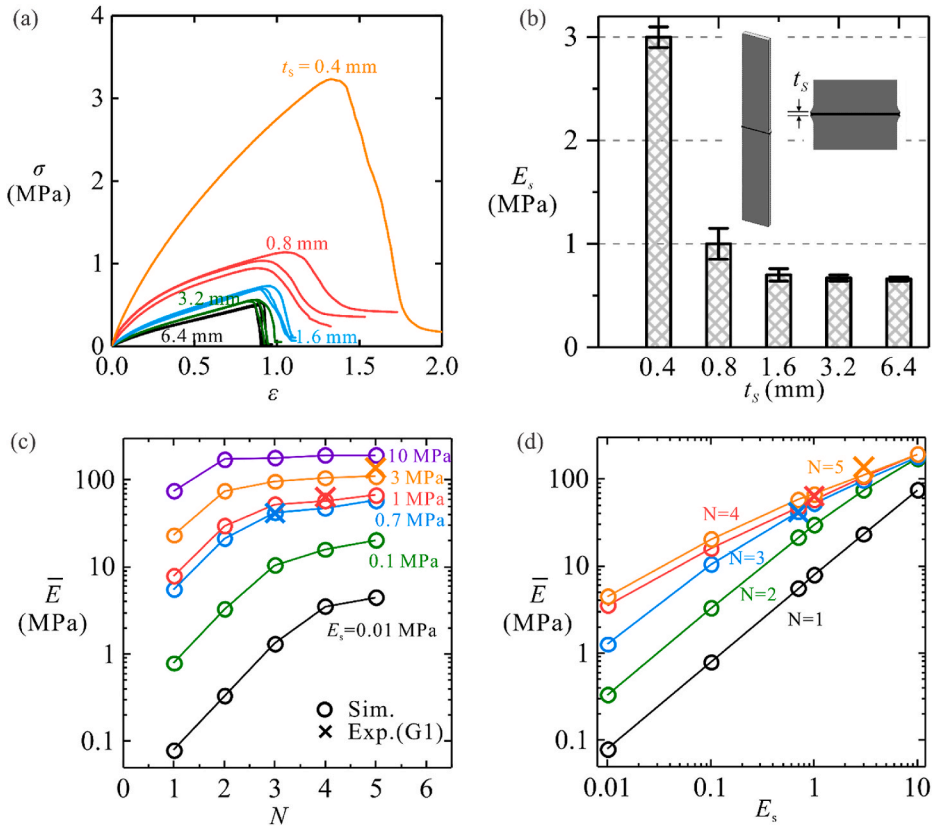

Fig. 8. The effect of stiffness ratio between hard phase and soft phase on the effective stiffness of space-filling fractal metamaterial. (a) The effective stiffness is a function of the hierarchy level, *N* under various stiffness ratios. (b) The effective stiffness as functions of the stiffness of soft phase under various hierarchy level, *N*.

Table 2
The effective stiffness of space-filling fractal metamaterial from experiments and simulations. The error between results from experiments and simulations is defined as $\left|\overline{E}_{sim}/\overline{E}_{exp}-1\right|$.

$\overline{E}$ (MPa)	G1 (f_S = 0.256)			G2 (t_N = 0.4 mm)		
	N = 3	N = 4	N = 5	N = 3	N = 4	N = 5
Experiment	41.72	63.86	136.98	249.05	180.30	136.98
Simulation	42.16	57.80	110.77	247.20	167.83	110.77
Error (%)	1.1	9.5	19.1	0.7	6.9	19.1

Here, ε is the overall strain and V is the total volume of the design. The total strain energy of the composite can be decomposed into the strain energy of the soft and hard phases:

$$U = U_s + U_h. \tag{2}$$

For the soft phase, the strain energy is:

$$U_s = \frac{1}{2}E_s\sum \varepsilon_i^2 V_i = \frac{1}{2}E_s\overline{\varepsilon_s}^2 V_s. \tag{3}$$

Similarly, the strain energy for the hard phase is

$$U_h = \frac{1}{2}E_h\overline{\varepsilon_h}^2 V_h, \tag{4}$$

where, $\overline{\varepsilon_s}$ and $\overline{\varepsilon_h}$ are the average strains for the soft phase and hard phase, respectively. V_s and V_h are the volume of the soft and hard phases, respectively. Here, we define the effective strain energy of the soft phase as:

$$\overline{U}_s = \overline{\varepsilon}_s^{\,2} = \frac{2U_s}{E_s V_s}. \tag{5}$$

Similarly, the effective strain energy of the hard phase is as

$$\overline{U}_h = \overline{\varepsilon}_h^{\,2} = \frac{2U_h}{E_h V_h}. \tag{6}$$

The effective strain energy of the composite is as

$$\overline{U} = \overline{\varepsilon}^2 = \frac{2U}{\overline{E}V}. \tag{7}$$

Substitute Eqs. (5)-(7) to Eq. (2), the normalized effective stiffness, $\overline{E}/E_h$ is

$$\frac{\overline{E}}{E_h} = f_s\frac{E_s}{E_h}\frac{\overline{U}_s}{\overline{U}} + (1-f_s)\frac{\overline{U}_h}{\overline{U}}. \tag{8}$$

Here, f_s is the volume fraction of the soft phase. The normalized effective stiffness of the composite is the sum of normalized effective strain energies from both the soft phase and hard phase.

Fixing the volume fraction of the soft phase, f_s, the normalized effective strain energies, $\overline{U}_s/\overline{U}$ and $\overline{U}_h/\overline{U}$ are functions of stiffness ratio, E_h/E_s and the hierarchy number, N, which have been obtained from the simulations, as shown in Fig. 9a and c, respectively. First, both $\overline{U}_h/\overline{U}$ and $\overline{U}_s/\overline{U}$ increase when increasing E_h/E_s. Second, $\overline{U}_h/\overline{U}$ increases with increasing N. When $E_h/E_s \le 2429$ and $N \ge 3$, $\overline{U}_h/\overline{U}$ keeps almost unchanged. In comparison, when $E_h/E_s \le 2429$ and $N \ge 2$, $\overline{U}_s/\overline{U}$ keeps almost unchanged. Furthermore, the von Mises stress contour of selected phases for N = 1, 3, and 5 has been shown in Fig. 9b and d. The stress contour in the hard phase increases with increasing E_h/E_s or increasing N (Fig. 8c). In comparison, the stress contour in the soft phase increases with increasing E_h/E_s and is independent of N. These results show that the stiffness ratio between hard and soft phases strongly affects the overall effective stiffness from strain energy analysis. However, the increasing hierarchy number mostly increases the stress in the hard

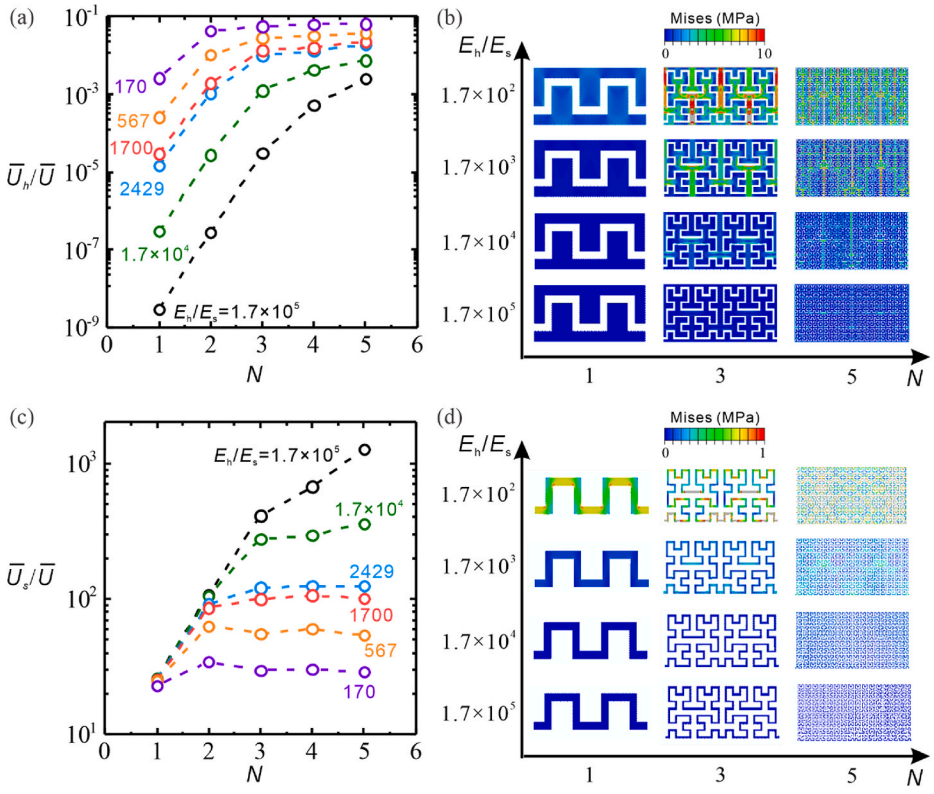

Fig. 9. The effect of stiffness ratio, E_h/E_s on the normalized effective stiffness. (a) The normalized effective strain energy, $\overline{U}_h/\overline{U}$ as a function of hierarchy number, N. (b) The von Mises stress contour of selected deformation pattern of hard phase under the overall tensile strain of 0.01. (c) The normalized effective strain energy, $\overline{U}_s/\overline{U}$ as a function of hierarchy number, N. (d) The von Mises stress contour of selected deformation pattern of hard phase under the overall tensile strain of 0.01.

phases which contributes to the increasing effective stiffness of composites.

The mechanical properties of space-filling fractal metamaterial is also affected by the volume fractions of hard phase and soft phase. From previous experimental results, the suture composite designs in G2 have the same soft interlayer thickness. Thus, the volume fraction of each phase is varied. For example, the volume fractions of the soft phase, f_s are 0.064, 0.128, and 0.256 for designs with $N = 3$, 4, and 5, respectively. Therefore, to study the effect of volume fraction on their overall properties, we performed another group of FE simulations of the suture composites with the volume fraction of the soft phase, $f_s = 0.50$, 0.256, 0.128, and 0.064. In all the designs, the thickness of the soft phase is 0.4 mm, meanwhile, the stiffness ratio is fixed as, $E_h/E_s = 567$. The effective stiffness measured from these simulations and previous experiments is shown in Fig. 10. First, the experiment data from G2 agrees well with the results from the simulations. Second, Fig. 10a shows at a certain volume fraction, a higher hierarchy number results in higher effective stiffness. However, the effective stiffness of composite tends to remain constant at larger hierarchy numbers ($N \geq 3$). Moreover, at a certain hierarchy number, smaller f_s results in higher effective stiffness, as shown in Fig. 10b. These results indicate that both the volume fraction and the hierarchy number strongly affect the overall stiffness of suture composites.

To further study the effect of volume fraction on each phase of the suture composite, the normalized effective strain energies, $\overline{U}_s/\overline{U}$ and $\overline{U}_h/\overline{U}$ are as functions of the volume fraction of the soft phase, f_s and the hierarchy number, N, is obtained from simulations and shown in Fig. 11a and c, respectively. First, both $\overline{U}_h/\overline{U}$ and $\overline{U}_s/\overline{U}$ increase when

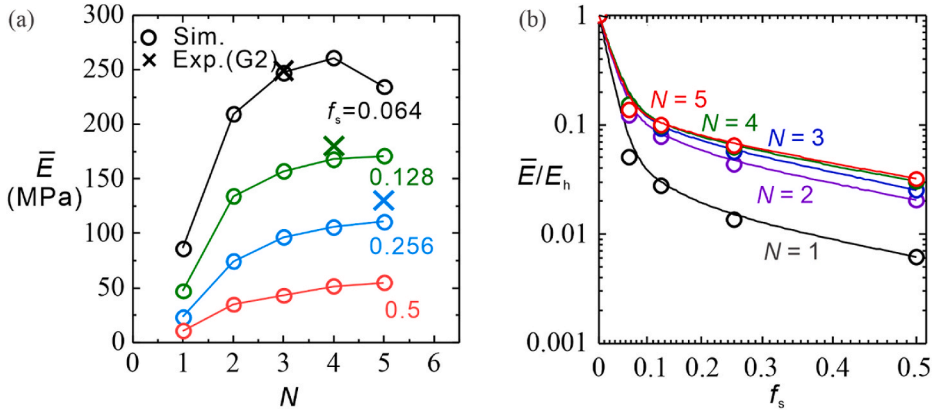

Fig. 10. The effect of volume fraction on the stiffness of space-filling fractal metamaterial. (a) The effective stiffness is a function of the hierarchy level, N under various volume fractions of hard phase. (b) The effective stiffness as functions of the volume fraction of hard phase under various hierarchy levels, N.

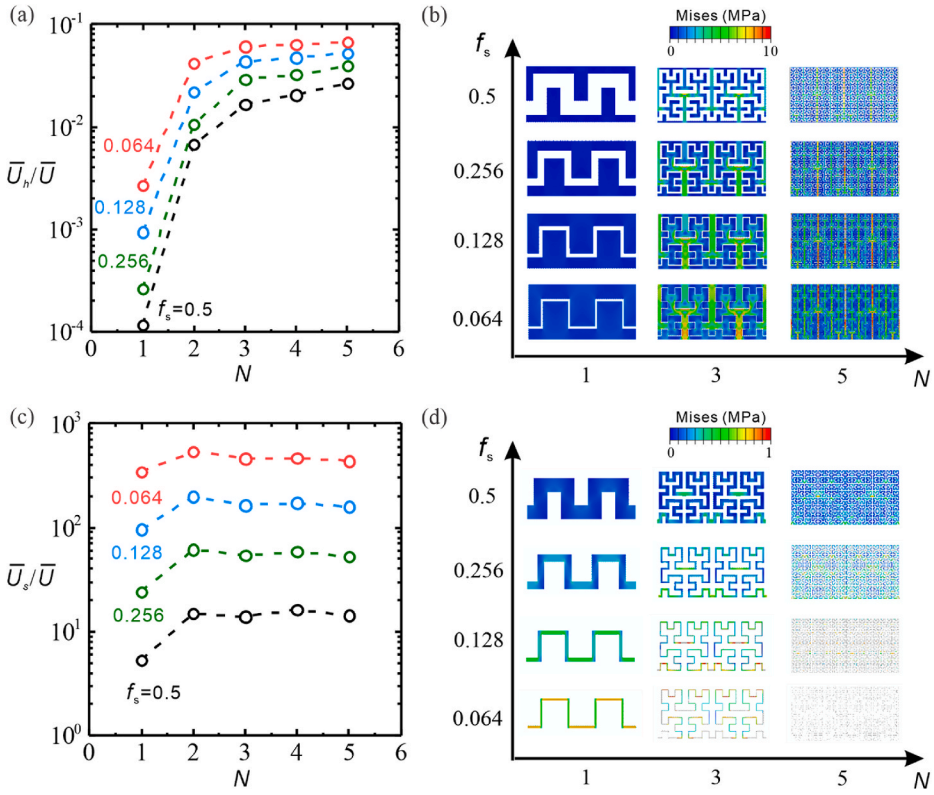

Fig. 11. The effect of volume fraction of both phases on the normalized effective stiffness. (a) The normalized effective strain energy, $\overline{U}_h/\overline{U}$ as a function of hierarchy number, *N*. (b) The von Mises stress contour of selected deformation pattern of hard phase under the overall tensile strain of 0.01. (c) The normalized effective strain energy, $\overline{U}_s/\overline{U}$ as a function of hierarchy number, *N*. (d) The von Mises stress contour of selected deformation pattern of hard phase under the overall tensile strain of 0.01.

decreasing f_s. Second, at a certain f_s, $\overline{U}_h/\overline{U}$ increases with increasing *N*. In comparison, at a certain f_s, $\overline{U}_s/\overline{U}$ keeps almost unchanged when $N \geq 2$. Furthermore, the von Mises stress contour of selected phases for $N = 1$, 3, and 5 has been shown in Fig. 11b and d. The stress contour in the hard phase increases with decreasing f_s or increasing *N* (Fig. 8c). In comparison, the stress contour in the soft phase increases with decreasing f_s and is independent of *N*. These results show that the volume fraction of each phase strongly affects the overall effective stiffness from strain energy analysis. However, the increasing hierarchy number mostly increases the stress in the hard phases which contributes to the increasing effective stiffness of composites.

5.2. Strength and resilience of space-filling fractal metamaterial

The strength and resilience of the suture composites is also affected by the hierarchy number and volume fraction of the hard phase. From previous experimental results (Section 4.1), we noticed that at early stage of stress-strain curves before the peak stress, most of the soft phase under stretching are pulled to break. And the left parts of the soft phase are under compression or shearing. The strength ratio between hard and soft constituent materials is larger than 40, here, $\sigma_h = 42$ MPa and $\sigma_s \leq 1$ MPa. Therefore, the contribution of the soft phase to the strength of the suture composites can be neglected. To study the strength and resilience of the suture composites numerically, we performed simulations on the suture composite designs without the soft phase. Here, we use an elastic-perfect-plastic material model to capture the behavior of hard phase material, VW. Its yield stress is modeled as, $\sigma_h = 42$ MPa. From these simulations, the strength and the resilience can be obtained as functions of hierarchy numbers as shown in Fig. 12a and b, respectively. First, we notice that at a certain volume fraction of the hard phase, the strength of the composites increases with increasing the hierarchy number. Apparently, at a certain hierarchy number, the composites with a higher volume fraction of hard phase have higher strength. The measured strength from the experiment agrees well with those measured from the simulations. Moreover, for resilience, it is noticed that, with increasing the hierarchy number, the composites have reached a higher resilience. Especially, the resilience of the composites seems independent of the volume fraction. Composites with various volume fractions have a close trend of the relations between resilience and hierarchy number. Furthermore, image snapshots at the maximum stress from the simulations and experiments are shown in Fig. 12c and d. We found that the locations where crack starts to occur in the experiment are the same ones where the stress is maximum in the simulations. This indicates that our simulations can predict not only the strength but also the locations of the crack start to propagate.

In general, the newly designed space-filling fractal metamaterial shows several differences compared with the conventional composite design from cellular material patterns. For cellular material patterns, there are two types. First, the cellular phase is hard and connected, while the inverse phase is empty or a softer material. This design is also known as a lattice-reinforced composite. Previous studies (Li et al., 2018, 2020; Li and Li, 2024) have shown that the properties of lattice-reinforced composites are dominated by the hard cellular phase, with the inverse soft matrix only providing limited additional contribution to the overall properties. Second, the cellular phase is made of connected soft materials, while the inverse phase is composed of harder materials. In these designs, the hard phase is separated into many isolated sections by the soft-connected lattices. One of our previous studies (Gao et al., 2018; Liu et al., 2020a) demonstrated that the properties of these designs are highly influenced by the deformation of the soft phase. In comparison, the currently designed space-filling fractal metamaterial features a more complex multi-phase geometry. These designs offer advantages over

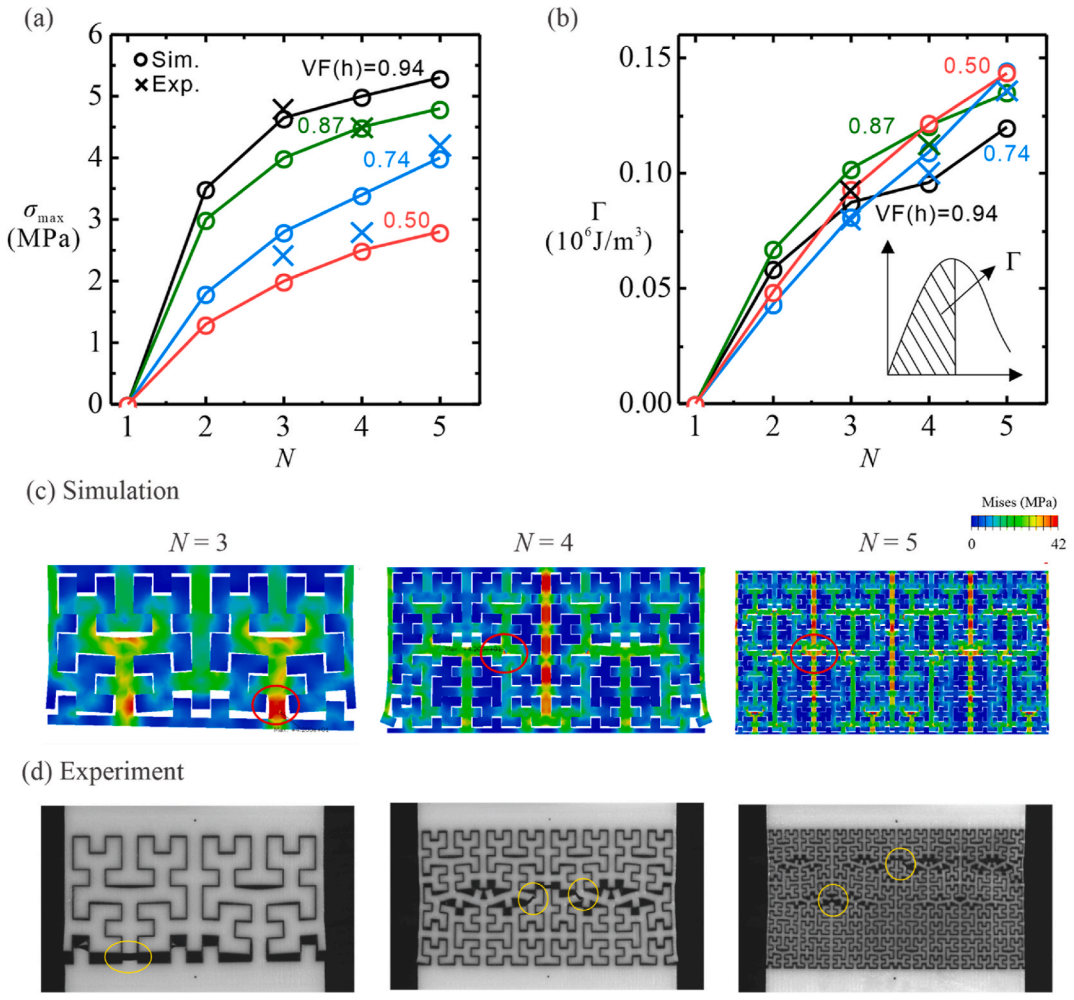

Fig. 12. The strength (a) and the resilience (b) as functions of hierarchy numbers at various volume fraction of the hard phase. Selected sample images at the maximum stress from simulations (c) and experiments (d).

both abovementioned types of cellular material patterns. Due to the space-filling fractal design, the new metamaterials can have increased interactions between the two phases and therefore can involve great contributions from both phased: the shear, compression, and tension of the soft phases, as well as the bending, stretching, interlocking of the hard phases. Consequently, both phases are more effectively taking the load and contribute to the overall deformation. Moreover, by rationally designing the fractal number, stiffness ratio of both phases, and the volume fraction of each phase, the overall mechanical properties can be significantly tuned.

6. Conclusion

In this paper, we design a new family of space-filling fractal metamaterial which is inspired from the complex microstructures of deer cranial sutures. These novel designs are generated from a mathematical fractal space-filling curve - Hilbert curves with a hierarchy number, *N* indicating the hierarchical/fractal level of the structures.

We use our multi-material 3D printer to fabricate these composite structures with N from 3 to 5. Tensile tests are performed to test their mechanical behaviors. We find that with increasing the hierarchical level, these suture composites have shown enhanced stiffness, strength, and resilience.

To study the effects of hierarchy number, stiffness ratio of multi-material, and volume fraction of each phase on the overall mechanical properties of these suture composites. We perform systematic simulations with various designs and constituent material properties. We found that with higher stiffness ratio and higher volume fraction of the hard phase will improve their stiffness and strength. However, the resilience is independent of the volume fraction of each phase. Our simulations can predict the mechanical properties which agree well with those from the experiments.

In general, these space-filling fractal metamaterials are a novel material design that has the potential to provide various applications including energy absorption materials, impact-resistant materials, and multi-functional materials.

CRediT authorship contribution statement

Tiantian Li: Writing – original draft, Visualization, Formal analysis. **Yaning Li:** Writing – review & editing, Validation, Supervision, Resources, Project administration, Methodology, Investigation, Funding acquisition, Conceptualization.

Declaration of competing interest

The authors declare that they have no known competing financial interests or personal relationships that could have appeared to influence the work reported in this paper.

Acknowledgments

We acknowledge the support from the start-up funds and SPARK award from Northeastern University and NSF through grants CMMI-2140223 and CMMI-2414457.

Data availability

Data will be made available on request.

References

Alheit, B., Bargmann, S., Reddy, B.D., 2020. Computationally modelling the mechanical behaviour of turtle shell sutures—a natural interlocking structure. J. Mech. Behav. Biomed. Mater. 110, 103973.
Arruda, E.M., Boyce, M.C., 1993. A three-dimensional constitutive model for the large stretch behavior of rubber elastic materials. J. Mech. Phys. Solid. 41, 389–412.
Cao, Y., Wang, W., Wang, J., Zhang, C., 2019. Experimental and numerical study on tensile failure behavior of bionic suture joints. J. Mech. Behav. Biomed. Mater. 92, 40–49.
Cui, S., Lu, Z., Yang, Z., He, X., 2021. Numerical investigation on the enhanced damping behavior of bio-inspired nacreous composites by introducing interlocked structure. J. Mech. Behav. Biomed. Mater. 119, 104442.
Dunlop, J.W.C., Weinkamer, R., Fratzl, P., 2011. Artful interfaces within biological materials. Mater. Today 14, 70–78.
Gao, C., Hasseldine, B.P.J., Li, L., Weaver, J.C., Li, Y., 2018. Amplifying strength, toughness, and auxeticity via wavy sutural tessellation in plant seedcoats. Adv. Mater. 30, 1800579.
Herring, S.W., 2008. Mechanical influences on suture development and patency. Front. Oral. Biol. 12, 41–56.
Hilbert, D., 1891. Ueber die stetige Abbildung einer Line auf ein Flächenstück. Math. Ann. 38, 459–460.
Hubbard, R.P., Melvin, J.W., Barodawala, I.T., 1971. Flexure of cranial sutures. J. Biomech. 4, 491–496.
Jaslow, C.R., 1990. Mechanical properties of cranial sutures. J. Biomech. 23, 313–321.
Jaslow, C.R., Biewener, A.A., 1995. Strain patterns in the horncores, cranial bones and sutures of goats (Capra hircus) during impact loading. J. Zool. 235, 193–210.
Krauss, S., Monsonego-Ornan, E., Zelzer, E., Fratzl, P., Shahar, R., 2009. Mechanical function of a complex three-dimensional suture joining the bony elements in the shell of the red-eared slider turtle. Adv. Mater. 21, 407–412.
Landman, N.H., Davis, R.A., Mapes, R.H., 2007. Cephalopods Present and Past: New Insights and Fresh Perspectives. Springer Science & Business Media.
Li, T., Chen, Y., Hu, X., Li, Y., Wang, L., 2018. Exploiting negative Poisson's ratio to design 3D-printed composites with enhanced mechanical properties. Mater. Des. 142, 247–258.
Li, T., Li, Y., 2024. Mechanical behaviors of three-dimensional chiral mechanical metamaterials. Compos. B Eng. 270, 111141.
Li, T., Liu, F., Wang, L., 2020. Enhancing indentation and impact resistance in auxetic composite materials. Compos. B Eng. 198, 108229.
Li, Y., Ortiz, C., Boyce, M.C., 2011. Stiffness and strength of suture joints in nature. Phys. Rev. 84, 062904.
Li, Y., Ortiz, C., Boyce, M.C., 2012. Bioinspired, mechanical, deterministic fractal model for hierarchical suture joints. Phys. Rev. 85, 031901.
Liu, F., Li, T., Jia, Z., Wang, L., 2020a. Combination of stiffness, strength, and toughness in 3D printed interlocking nacre-like composites. Extr. Mech. Lett. 35, 100621.
Liu, F., Li, T., Jiang, X., Jia, Z., Xu, Z., Wang, L., 2020b. The effect of material mixing on interfacial stiffness and strength of multi-material additive manufacturing. Addit. Manuf. 36, 101502.
Liu, L., Li, Y., 2018. Predicting the mixed-mode I/II spatial damage propagation along 3D-printed soft interfacial layer via a hyperelastic softening model. J. Mech. Phys. Solid. 116, 17–32.
Long, C.A., Long, J.E., 2008. Fractal dimensions of cranial sutures and waveforms. Acta Anat. 145, 201–206.
Martínez-Magallanes, M., Cuan-Urquizo, E., Crespo-Sánchez, S.E., Valerga, A.P., Roman-Flores, A., Ramírez-Cedillo, E., Treviño-Quintanilla, C.D., 2023. Hierarchical and fractal structured materials: design, additive manufacturing and mechanical properties. Proc. Inst. Mech. Eng., Part L 237, 650–666.
Martínez-Magallanes, M., Perez-Santiago, R., Roman-Flores, A., Cuan-Urquizo, E., 2024. Flexural properties of additively manufactured structures reinforced with cellular and fractal patterns. Adv. Eng. Mater. 26, 2301938.
Meyers, M.A., Chen, P.-Y., Lin, A.Y.-M., Seki, Y., 2008. Biological materials: structure and mechanical properties. Prog. Mater. Sci. 53, 1–206.
Nicolay, C.W., Vaders, M.J., 2006. Cranial suture complexity in white-tailed deer (Odocoileus virginianus). J. Morphol. 267, 841–849.
Saunders, W.B., Work, D.M., 1996. Shell morphology and suture complexity in upper carboniferous ammonoids. Paleobiology 22, 189–218.
Saunders, W.B., Work, D.M., Nikolaeva, S.V., 1999. Evolution of complexity in paleozoic ammonoid sutures. Science 286, 760–763.
Song, J., Reichert, S., Kallai, I., Gazit, D., Wund, M., Boyce, M.C., Ortiz, C., 2010. Quantitative microstructural studies of the armor of the marine threespine stickleback (Gasterosteus aculeatus). J. Struct. Biol. 171, 318–331.
Sun, Z., Lee, E., Herring, S.W., 2004. Cranial sutures and bones: growth and fusion in relation to masticatory strain. The Anatomical Record Part A: discoveries in Molecular. Cellul. Evolut. Biol. 276A, 150–161.
Wainwright, S.A., 1982. Mechanical Design in Organisms. Princeton University Press.
Wang, W., Sun, Y., Lu, Y., Wang, J., Cao, Y., Zhang, C., 2021. Tensile behavior of bio-inspired hierarchical suture joint with uniform fractal interlocking design. J. Mech. Behav. Biomed. Mater. 113, 104137.
Yao, H., Gao, H., 2006. Mechanics of robust and releasable adhesion in biology: bottom–up designed hierarchical structures of gecko. J. Mech. Phys. Solid. 54, 1120–1146.
Zhang, Z., Jiang, H., Bednarcyk, B.A., Chen, Y., 2023. Greek key inspired fractal metamaterials with superior stretchability for tunable wave propagation. Adv. Mater. Technol. 8, 2300981.
Zhou, H., Zhang, Y., 2005. Hierarchical chain model of spider capture silk elasticity. Phys. Rev. Lett. 94, 028104.